

TECHNICAL REPORT
NATICK/TR-13/002



AD _____

APERIODIC PHOTONIC-PLASMONIC STRUCTURES WITH BROADBAND FIELD ENHANCEMENT

by
Gary Walsh
and
Luca Dal Negro

Boston University
Boston, MA 02215-2421

October 2012

Final Report
September 2009 – September 2010

Approved for public release; distribution is unlimited

Prepared for
U.S. Army Natick Soldier Research, Development and Engineering Center
Natick, Massachusetts 01760-5020

UNCLASSIFIED

DISCLAIMERS

The findings contained in this report are not to be construed as an official Department of the Army position unless so designated by other authorized documents.

Citation of trade names in this report does not constitute an official endorsement or approval of the use of such items.

DESTRUCTION NOTICE

For Classified Documents:

Follow the procedures in DoD 5200.22-M, Industrial Security Manual, Section II-19 or DoD 5200.1-R, Information Security Program Regulation, Chapter IX.

For Unclassified/Limited Distribution Documents:

Destroy by any method that prevents disclosure of contents or reconstruction of the document.

UNCLASSIFIED

REPORT DOCUMENTATION PAGE

Form Approved
OMB No. 0704-0188

Public reporting burden for this collection of information is estimated to average 1 hour per response, including the time for reviewing instructions, searching existing data sources, gathering and maintaining the data needed, and completing and reviewing this collection of information. Send comments regarding this burden estimate or any other aspect of this collection of information, including suggestions for reducing this burden to Department of Defense, Washington Headquarters Services, Directorate for Information Operations and Reports (0704-0188), 1215 Jefferson Davis Highway, Suite 1204, Arlington, VA 22202-4302. Respondents should be aware that notwithstanding any other provision of law, no person shall be subject to any penalty for failing to comply with a collection of information if it does not display a currently valid OMB control number.

PLEASE DO NOT RETURN YOUR FORM TO THE ABOVE ADDRESS.

1. REPORT DATE (DD-MM-YYYY) 15-10-2012		2. REPORT TYPE Final		3. DATES COVERED (From - To) September 2009 –September 2010													
4. TITLE AND SUBTITLE APERIODIC PHOTONIC-PLASMONIC STRUCTURES WITH BROADBAND FIELD ENHANCEMENT			5a. CONTRACT NUMBER W911NF-07-D-0001														
			5b. GRANT NUMBER														
			5c. PROGRAM ELEMENT NUMBER														
6. AUTHOR(S) Gary Walsh and Luca Dal Negro			5d. PROJECT NUMBER														
			5e. TASK NUMBER														
			5f. WORK UNIT NUMBER														
7. PERFORMING ORGANIZATION NAME(S) AND ADDRESS(ES) Boston University 8 Saint Mary's Street Boston, MA 02215-2421			8. PERFORMING ORGANIZATION REPORT NUMBER														
9. SPONSORING / MONITORING AGENCY NAME(S) AND ADDRESS(ES) U.S. Army Natick Soldier Research, Development and Engineering Center ATTN: RDNS-WSB-N (L. Hoke) Kansas Street, Natick, MA 01760-5020			10. SPONSOR/MONITOR'S ACRONYM(S) NSRDEC														
			11. SPONSOR/MONITOR'S REPORT NUMBER(S) NATICK/TR-13/002														
12. DISTRIBUTION / AVAILABILITY STATEMENT Approved for public release; distribution is unlimited.																	
13. SUPPLEMENTARY NOTES The contractor is Battelle Memorial Institute, 505 King Avenue, Columbus, OH 43201. Boston University is a subcontractor to Battelle.																	
14. ABSTRACT This report documents project work performed by Boston University (BU) under a contract awarded by the Natick Soldier Research, Development and Engineering Center (NSRDEC) to Battelle Memorial Institute. The project was aimed at combining plasmonic field enhancement effects in rigorously designed metal-dielectric arrays of nanoparticles with periodic and aperiodic geometries for the demonstration of field-enhanced isomerization with minimum background absorption. BU developed metal-dielectric nanostructures on transparent substrates (quartz, silicon nitride) which can create plasmonic field enhancement engineered over broad frequency bands, while minimizing linear absorption of anisotropic dyes. Based on coupled dipoles and rigorous null-field theory (T-matrix) calculations, BU discovered and explained the fundamental mechanisms governing broadband plasmonic scattering and near-field enhancement in a number of plasmonic structures. A large number of photonic-plasmonic structures with different geometries (from periodic to quasi-periodic and pseudo-random) have been designed by rigorous electrodynamics theory for maximum enhancement at 532nm. BU then fabricated all the structures using Electron beam Lithography, explored the respective roles of morphology, particle shapes, size, and correlated their theory with experiments by dark field scattering spectroscopy and depolarization ellipsometry. The nonlinear optical properties of Azobenzene Doped Polymers was quantified, and integration of limiting devices with micro-fluidics technology was explored. Finally, a plasmonic scatterometer was designed, built, and tested for the accurate measurement of the angular scattering profiles and radiation diagrams of complex nanoplasmonic structures.																	
15. SUBJECT TERMS <table style="width: 100%; border: none;"> <tr> <td style="width: 33%;">ARRAYS</td> <td style="width: 33%;">ISOMERIZATION</td> <td style="width: 33%;">PLASMONIC STRUCTURES</td> </tr> <tr> <td>PLASMONS</td> <td>NANOPARTICLES</td> <td>NEAR-FIELD ENHANCEMENT</td> </tr> <tr> <td>BROADBAND</td> <td>NANOPLASMONICS</td> <td>APERIODIC PHASED ARRAYS</td> </tr> <tr> <td>APERIODICITY</td> <td>APERIODIC ARRAYS</td> <td>ELECTRON BEAM LITHOGRAPHY</td> </tr> </table>						ARRAYS	ISOMERIZATION	PLASMONIC STRUCTURES	PLASMONS	NANOPARTICLES	NEAR-FIELD ENHANCEMENT	BROADBAND	NANOPLASMONICS	APERIODIC PHASED ARRAYS	APERIODICITY	APERIODIC ARRAYS	ELECTRON BEAM LITHOGRAPHY
ARRAYS	ISOMERIZATION	PLASMONIC STRUCTURES															
PLASMONS	NANOPARTICLES	NEAR-FIELD ENHANCEMENT															
BROADBAND	NANOPLASMONICS	APERIODIC PHASED ARRAYS															
APERIODICITY	APERIODIC ARRAYS	ELECTRON BEAM LITHOGRAPHY															
16. SECURITY CLASSIFICATION OF:			17. LIMITATION OF ABSTRACT	18. NUMBER OF PAGES	19a. NAME OF RESPONSIBLE PERSON												
a. REPORT	b. ABSTRACT	c. THIS PAGE			Landa Hoke												
U	U	U	SAR	36	19b. TELEPHONE NUMBER (include area code) 508-233-4588												

This page intentionally left blank

UNCLASSIFIED

TABLE OF CONTENTS

List of Figures	iv
1. Introduction	1
2. Design	2
2.1. <i>Prime Number Arrays</i>	2
2.2. <i>Particle Swarm Optimized Arrays</i>	2
2.3. <i>Wood's Anomaly</i>	3
2.4. <i>Chirped Arrays</i>	4
2.5. <i>Generalization of Photonic-Plasmonic Coupling</i>	8
3. Experimental Activities	13
3.1. <i>Depolarization Ellipsometry</i>	13
3.2. <i>Optical Limiting</i>	15
3.3. <i>Enhancement of Kerr Nonlinearities in Azobenzene Doped Polymers</i>	20
4. Instruments	24
4.1. <i>Scatterometer</i>	24
Publications	27
References	27

LIST OF FIGURES

Fig 1. Maximum field enhancement versus the wavelength for an isolated particle, and for periodic, coprime, prime, and Ulam arrays. The arrays are excited by a circularly polarized plane wave at normal incidence.....	2
Fig 2. Maximum field enhancement $ E $ spectra of the optimized arrays of gold (a) and silver (b) nanoparticles, illuminated, at normal incidence, by a circularly polarized plane wave of unitary intensity.....	3
Fig 3. (a) Maximum field enhancement of a dimer of 100 nm diameter silver spheres with various edge-to edge-separation indicated by the color. (b) Same dimers arranged in a triangular periodic lattice with lattice constant 550 nm. (c) and (d) Scaling of maximum field enhancement with dimer edge-to-edge separation for single dimer and the array.	4
Fig 4. (a) Linearly chirped square array of dimers. (b) Maximum field enhancement spectrum of chirped array.	5
Fig 5. Bases for chirped photonic plasmonic arrays.....	5
Fig 6. (a) Scattering efficiency and (b) maximum field enhancement spectra of three isolated bases.....	5
Fig 7. One-dimensionally chirped rectangular arrays of (a) monomers, (b) dimers, (c) trimers. The scattering efficiency and maximum field enhancement respectively of (c and f) monomer, (d and g) dimer, (e and i) trimer.	6
Fig 8. Near-field enhancement factor (max field enhancement of array divided by that of isolated base) of all three arrays.....	7
Fig 9. (a) Scattering efficiency, (b) maximum field enhancement, and (c) near-field enhancement factor of chirped line with $N = 100$	7
Fig 10. X position of the maximum field enhancement as a function of wavelength for both arrays, $N = 15$ and $N = 100$	8
Fig 11. Condition for in-plane scattering.....	9
Fig 12. Wood's anomaly condition for (a) periodic, (b) Fibonacci, (c) Thue-Morse, (d) Rudin-Shapiro arrays at three different normalized wavelengths.....	10
Fig 13. Graphical description of radial distribution function.....	11
Fig 14. The components of the radial distribution function. (a-d) numerator, (e-h) denominator, (i-l) entire radial distribution function.....	11
Fig 15. Radial distribution function of four arrays.....	12

Fig 16: (a) Schematic of ellipsometry experiment. (b) Ellipsometric parameters Ψ and Δ for an array of gold dimers illuminated at 60° . (c) Depolarization of an array of dimers and monomers. (d) Depolarization of arrays of dimers with various minimum inter-particle separation indicated in the legend. Scaling of maximum depolarization with minimum separation (inset).	13
Fig 17: (a) Simulated depolarization for chains of dimers with various separation compared to that of monomers and an isolated dimer. (b) Scaling of the maximum depolarization with minimum separation.....	14
Fig 18. SEMs of 100 nm gold cylinder arrays of quartz. (a) triangular dimer with 530 nm lattice constant, (b) Fibonacci, (c) designed structure with particle swarm optimization.	15
Fig 19. Schematics of limiting experiments. (a) Pulsed pump-probe: the two analyzers are crossed. The LC sample rotates the polarization when it is in the nematic phase. Time dynamics of the CW probe laser are measured on the power meter as a single pulse from the pump laser caused the LC to transition to the isotropic phase leading to zero transmission through the cross analyzers. (b) CW limiting setup: the two analyzers are crossed. A mechanical shutter opens and the time dynamics of the transmission of the CW 530 nm laser are measured on the power meter as the LC switches from its nematic to isotropic phase.	16
Fig 20. Pump-probe results. (a) Fibonacci array, (b) no array. Pump red, probe blue. Probe normalized to its maximum. (c) comparison on probe from (a) & (b) in unnormalized units. ...	17
Fig 21. Optical density of four LC samples. Samples 1 and 2 have arrays and were made for us by Natick. Sample 3 has arrays that we made. The existing sample was made by Natick by rubbing back and forth to remove excess dye.....	17
Fig 22. Time dynamics of CW limiting experiments from the existing sample. Input power is changed.	18
Fig 23. Steps for fabricating micro-fluidic channels around plasmonic arrays.....	19
Fig 24. (a) Photoresist mold to make the PDMS channel. (b) PDMS channel on a quartz substrate.	20
Fig 25. Spin speed calibration of 5% DR1, 95% PMMA by weight in a 2.6% solution of anisole:toluene 1:1	21
Fig 26. Zscan setup	21
Fig 27. Theoretical close aperture zscan data.....	22
Fig 28. Optical density measurements of the DR1 doped PMMA films.....	23
Fig 29. Un-normalized zscan data from DR1 doped PMMA film	23
Fig 30. Schematic of scatterometer	24

Fig 31. Scatterometer full system	25
Fig 32. Automated variation of collection angle	25
Fig 33. System with automated variable analyzer	26
Fig 34. System with automated variable phase retarder	26

APERIODIC PHOTONIC-PLASMONIC STRUCTURES WITH BROADBAND FIELD ENHANCEMENT

1. Introduction

This report documents project work performed by Boston University, between September 2009 and September 2010, under a contract (W911NF-07-D-0001) awarded to the Battelle Memorial Institute by the Natick Soldier Research, Development and Engineering Center (NSRDEC). The project was aimed at combining plasmonic field enhancement effects in rigorously designed metal-dielectric arrays of nanoparticles with periodic and aperiodic geometries for the demonstration of field-enhanced isomerization with minimum background absorption. The objective was to develop metal-dielectric nanostructures on transparent substrates (quartz, silicon nitride) which can create the largest possible field enhancement engineered over broad frequency bands, while minimizing linear absorption of anisotropic dyes. Based on coupled dipoles and rigorous null-field theory (T-matrix) calculations, we discovered and explained the fundamental mechanisms governing broadband plasmonic scattering and near-field enhancement in a number of plasmonic structures. A large number of photonic-plasmonic structures with different geometries (from periodic to quasi-periodic and pseudo-random) have been designed by rigorous electrodynamics theory for maximum enhancement at 532nm and investigated experimentally. Based on our modeling, we built an intuitive Fourier optics approach to Wood's anomalies in nanoplasmonics and demonstrated for the first time [1-3] large and controllable field enhancement effects spanning across the entire visible band, as discussed below. We then fabricated all the structures using electron beam lithography, explored the respective roles of morphology, particle shapes, and size, and correlated our theory with experiments by dark field scattering spectroscopy and spectroscopic ellipsometry. We quantified the nonlinear optical properties (nonlinear index) of azobenzene doped polymers and explored the integration of limiting devices with micro-fluidics technology. Finally, we designed, built and tested a novel instrument, which we call a plasmonic scatterometer, for the accurate measurement of the angular scattering profiles and radiation diagrams of complex nanoplasmonic structures (see the details in the Instrument section). All these steps are articulated along several stages of design, fabrication and experimental characterization, as detailed in the following sections.

2. Design

2.1. Prime Number Arrays

Using a recently developed coupled dipole approximation (CDA) model [1], we have optimized the procedures for calculating the near and far field patterns of arrays of metal and dielectric nano-spheres embedded in a uniform medium, and defined novel figures of merit for the broadband plasmonic response of aperiodic arrays.

We used the CDA model to perform a theoretical study of a novel class of plasmonic arrays based on the distribution of prime numbers. We have demonstrated a much larger maximum field enhancement over a broader frequency range in these structures than in similar square periodic arrays, as shown in Fig. 1. Further, we have demonstrated that the surface area of these arrays covered by enhanced plasmonic fields (hot spots) is larger than in reference periodic systems. We have also explained the near field and far field scattering regimes of these novel plasmonic structures and understood general structural/property relations. For more details see our paper published in Optics Express [publication 1].

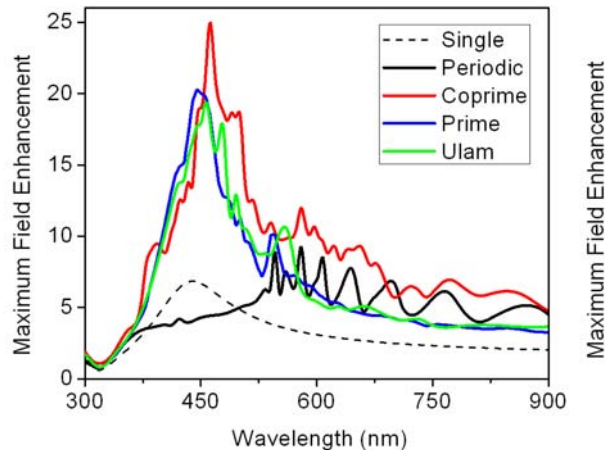


Fig 1. Maximum field enhancement versus the wavelength for an isolated particle, and for periodic, coprime, prime, and Ulam arrays. The arrays are excited by a circularly polarized plane wave at normal incidence.

2.2. Particle Swarm Optimized Arrays

Through an international collaboration with Dr. Massimo Donelli at the University of Trento in Italy, we have interfaced our CDA numerical code with a particle swarm optimization (PSO) algorithm and used this to design the structural geometry of plasmonic arrays of gold and silver nanoparticles for maximum field enhancement at 532 nm and across a broad frequency band spanning the entire visible spectrum. Fig. 2 shows the maximum field enhancement spectrum of these arrays. For more details see our Optics Letters paper [publication 2].

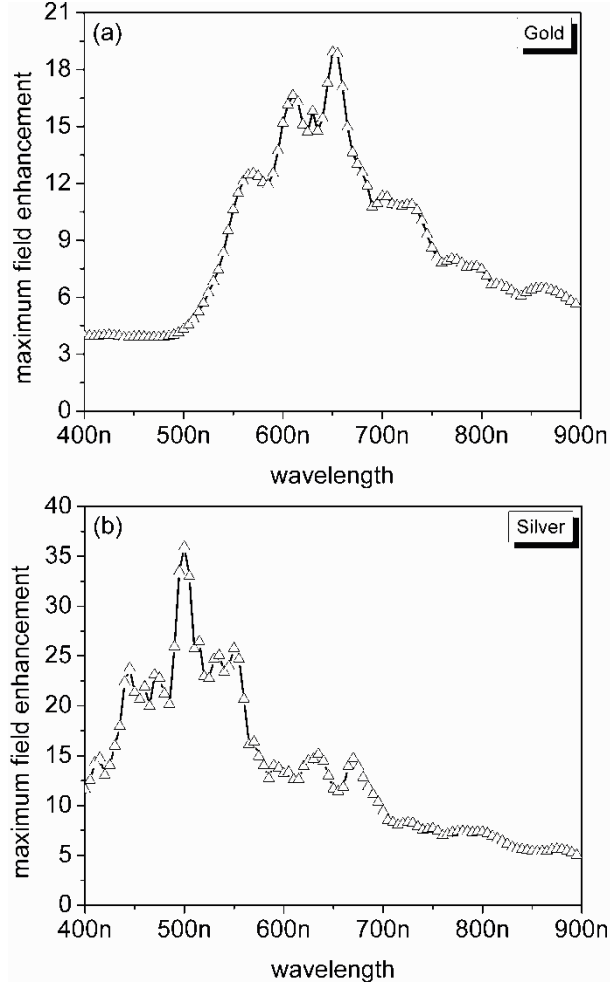


Fig 2. Maximum field enhancement $|E|$ spectra of the optimized arrays of gold (a) and silver (b) nanoparticles, illuminated, at normal incidence, by a circularly polarized plane wave of unitary intensity.

2.3. Wood's Anomaly

Using our CDA model, we have demonstrated that it is possible to use the Wood's anomaly to feed the strong near field enhancement observed in small clusters of metallic nanoparticles at designed spectral positions. Fig. 3 illustrates this designable enhancement in a triangular array of silver dimers. Equation 1 specifies the Wood's anomaly condition [2].

$$\lambda_o = \frac{a}{m} n \sin \theta_{inc} \quad (1)$$

Where, a is the lattice constant, n is the refractive index of the surrounding medium, θ_{inc} is the angle of incidence, and m is an integer. For normal incidence ($\theta_{inc} = 90^\circ$) in freespace ($n = 1$) and selecting the first diffractive order ($m = 1$), Equation 1 becomes,

$$\lambda_o = a \quad (2)$$

When this condition is met the first diffracted order feeds into the strong dimer plasmonic resonance creating a narrow peak in the field enhancement spectrum.

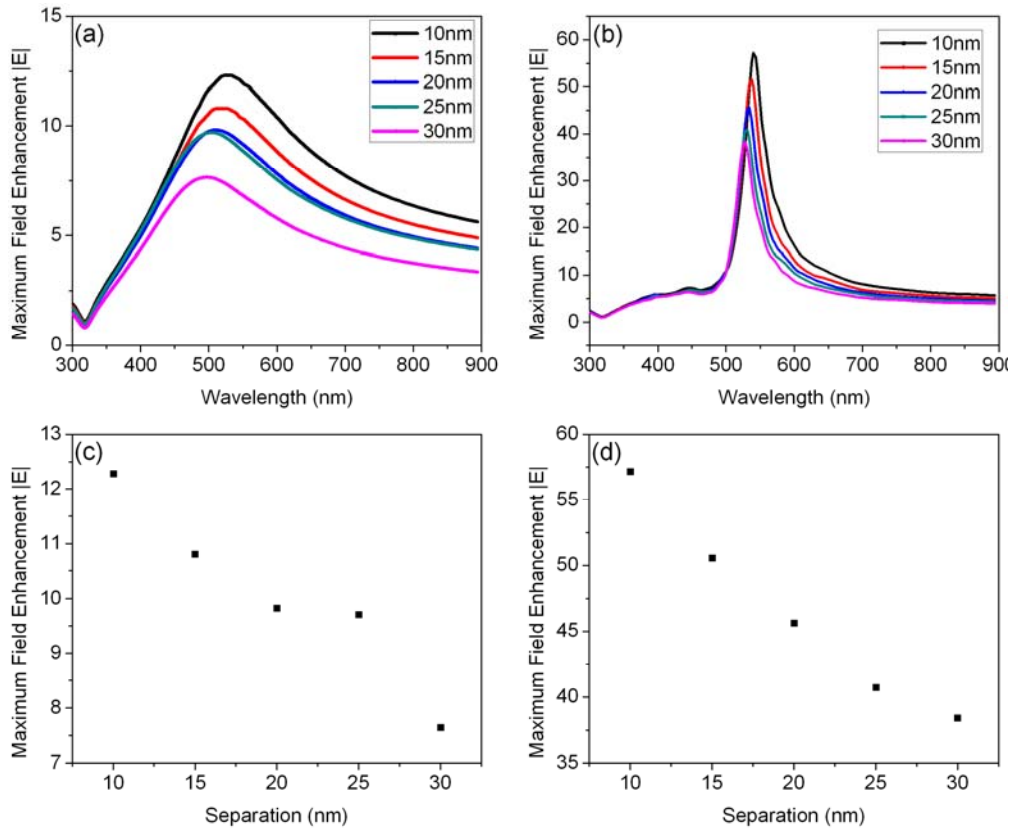


Fig 3. (a) Maximum field enhancement of a dimer of 100 nm diameter silver spheres with various edge-to-edge separation indicated by the color. (b) Same dimers arranged in a triangular periodic lattice with lattice constant 550 nm. (c) and (d) Scaling of maximum field enhancement with dimer edge-to-edge separation for single dimer and the array.

This work spared a study using periodic arrays of dimers using depolarization ellipsometry. A discussion of these activities can be found in the Experiments section of this report. This work has produced a paper which will be submitted to Nano Letters for publication. We used a more advanced semi-analytical tool for the theory of this paper, the description of which is included with the experiment for the sake of clarity.

2.4. Chirped Arrays

Expanding on the concept of Wood's anomaly, we have designed an array with a broadband plasmonic response by chirping a square periodic lattice of dimers. Fig. 4 shows an array of 100 nm diameter silver dimers with 25 nm edge-to-edge separation with the lattice constant linearly chirped between 400 and 700 nm and its corresponding field enhancement spectrum (a). Here, the local near uniform spacing of adjacent dimers causes the Wood's anomaly condition to be met over a large frequency band.

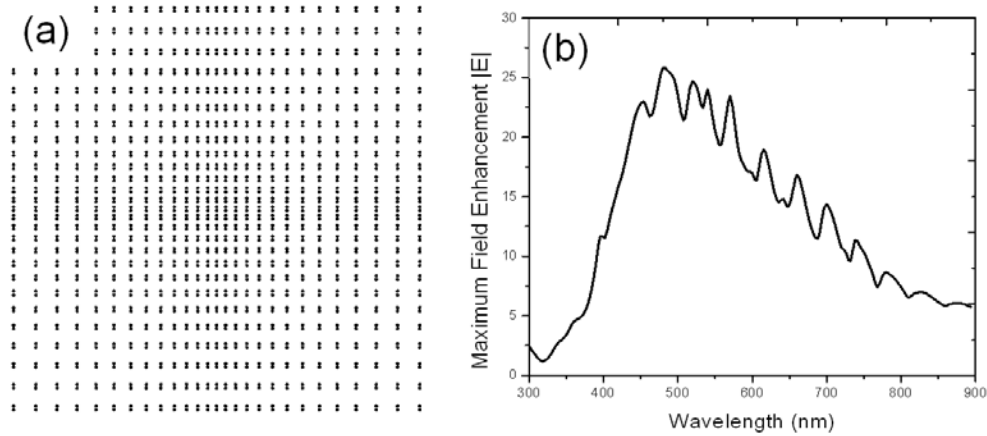


Fig 4. (a) Linearly chirped square array of dimers. (b) Maximum field enhancement spectrum of chirped array.

Further expanding this work we investigated the role of the lattice base element of the photonic-plasmonic response. This analysis uses three bases; monomers, dimers, and trimers shown in Fig 5. In our analysis we used silver spheres with 100 nm diameter and a minimum separation within the bases of 25 nm.

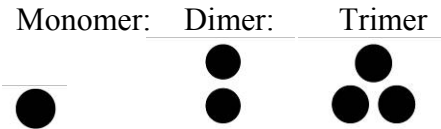


Fig 5. Bases for chirped photonic plasmonic arrays

Fig 6 shows the scattering efficiency and maximum field enhancement spectra calculated for each of these bases when illuminated with a normally incident plane wave polarized in the Y direction (along the axis of the dimer in Fig 3).

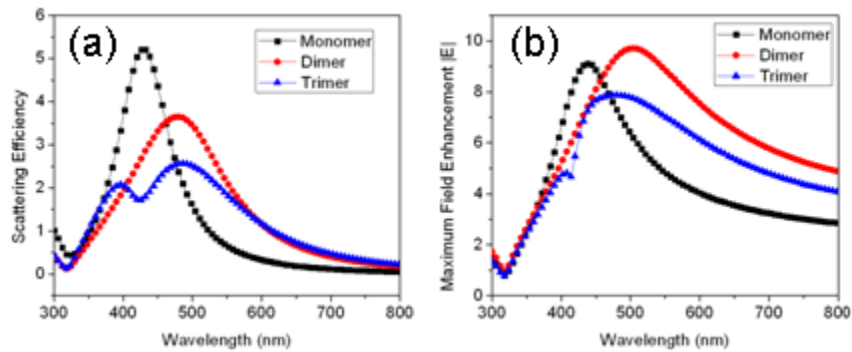


Fig 6. (a) Scattering efficiency and (b) maximum field enhancement spectra of three isolated bases.

We reduced the complexity of the array by chirping in only one direction (+X) and holding the spacing in the other direction (Y) constant. Fig 7 a-c show these one-dimensional chirped arrays for the three different bases. The arrays are linearly chirped in the +X direction from 400 – 700 nm with $N = 15$ columns. The slope of the chirping is 21.4 nm/column. The spacing in the Y direction is 400 nm. Fig 7 d-i shows the scattering efficiency and maximum field enhancement of each array compared with that of the isolated base.

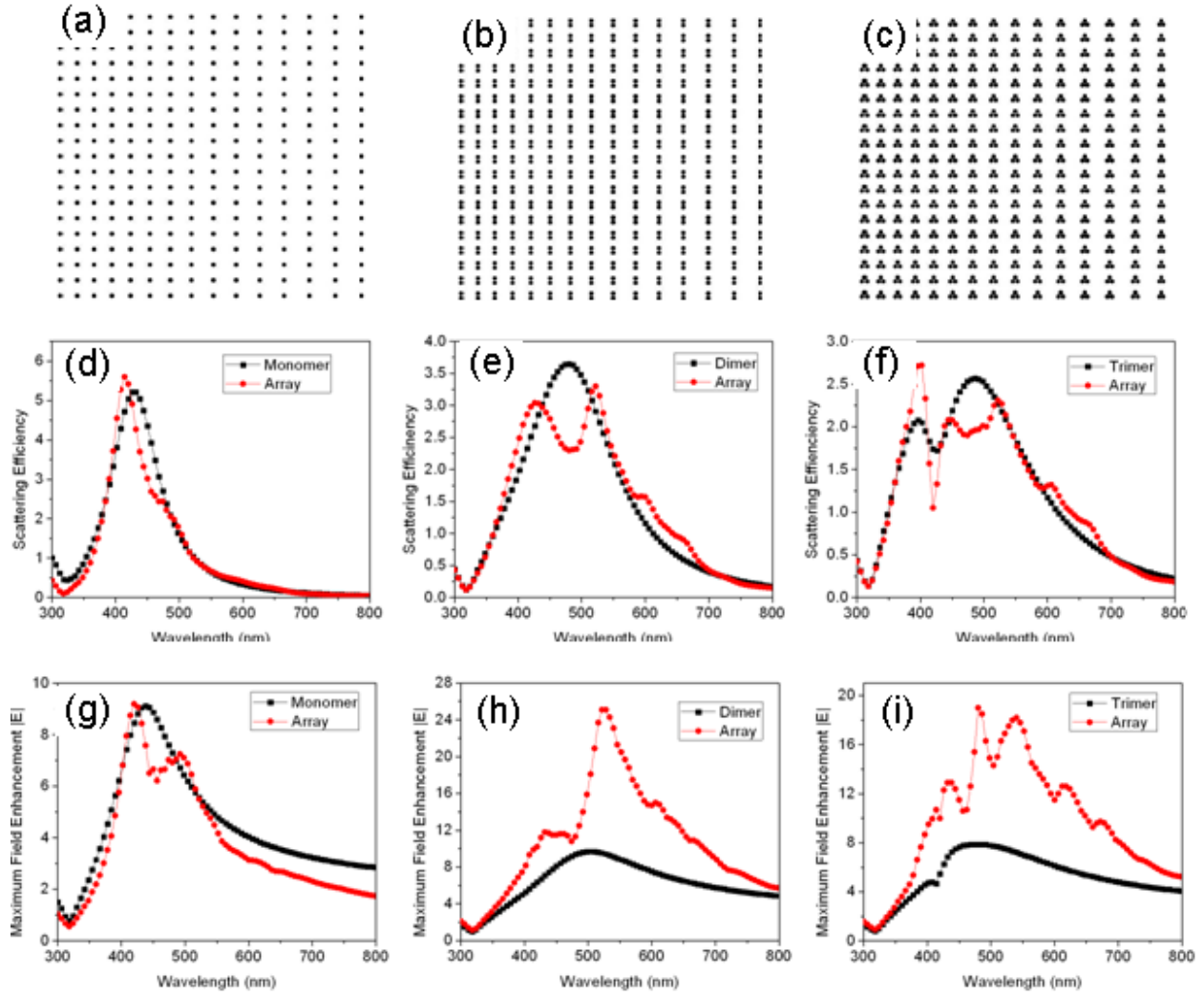


Fig 7. One-dimensionally chirped rectangular arrays of (a) monomers, (b) dimers, (c) trimers. The scattering efficiency and maximum field enhancement respectively of (c and f) monomer, (d and g) dimer, (e and i) trimer.

We define the near-field enhancement factor as the ratio of the maximum field enhancement spectrum of the array to that of the isolated base. This value is plotted for the three arrays in Fig 8. Notice that even though the maximum field enhancement spectra for the dimer and trimer (Fig 7 h and i) do not appear to be similar, their enhancement factors, particularly in the 500-900 nm range, are almost identical. This indicates that there is some underlying array function which may be able to be used to predict the maximum field enhancement spectrum from that of the isolated base.

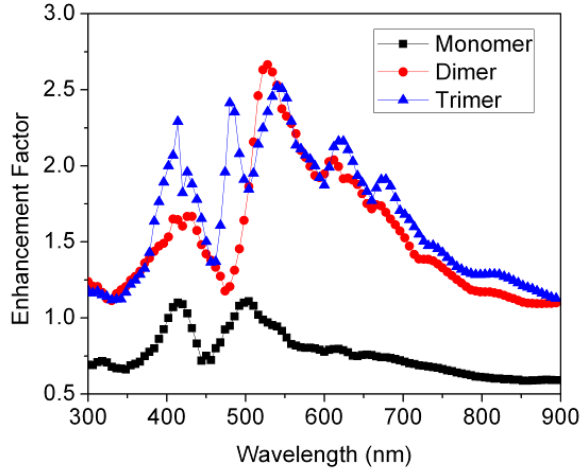


Fig 8. Near-field enhancement factor (max field enhancement of array divided by that of isolated base) of all three arrays.

Finally, we investigated the position of the field maxima at various wavelengths. We simulated chains of silver dimers linearly chirped from 500 to 700 nm with the number of dimers $N = 15$ and 100, which translates to slopes of 21.4 nm/column and 3 nm/column respectively. The results are shown in Fig 9. There is almost no difference in the scattering efficiency of two linear arrays, but the longer chain has a much higher field enhancement due to the more long range feedback from the nearly momentum matching properties of the chirped array.

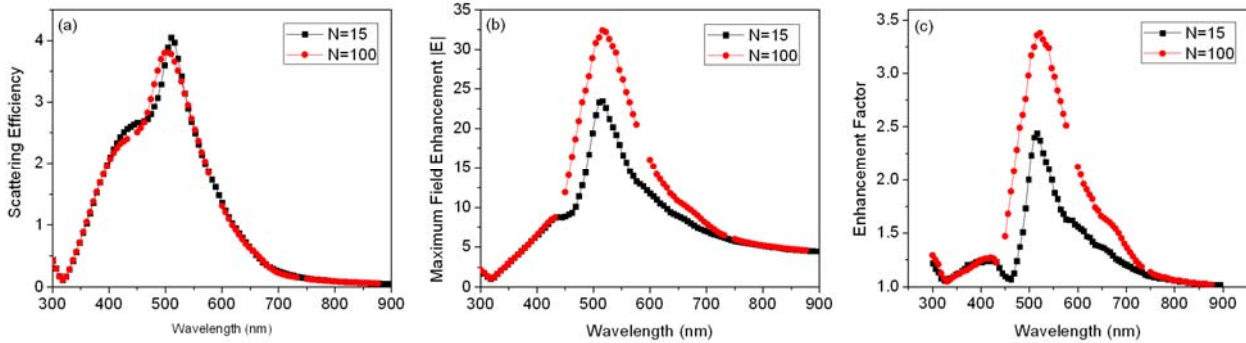


Fig 9. (a) Scattering efficiency, (b) maximum field enhancement, and (c) near-field enhancement factor of chirped line with $N = 100$.

Our theory is that chirping the grating creates a type of quasi-Wood's anomaly at all the wavelengths in the chirping range. If this is true, then the X position of the maximum field enhancement should change linearly with wavelength. Fig10 shows the X positions of the maximum field enhancement for each of the line arrays ($N = 15$ and $N = 100$). We see indeed that this curve varies linearly between 400 and 700 nm. If these results can be experimentally realized it means that we can engineer the exact location of hot spots over a broad frequency range.

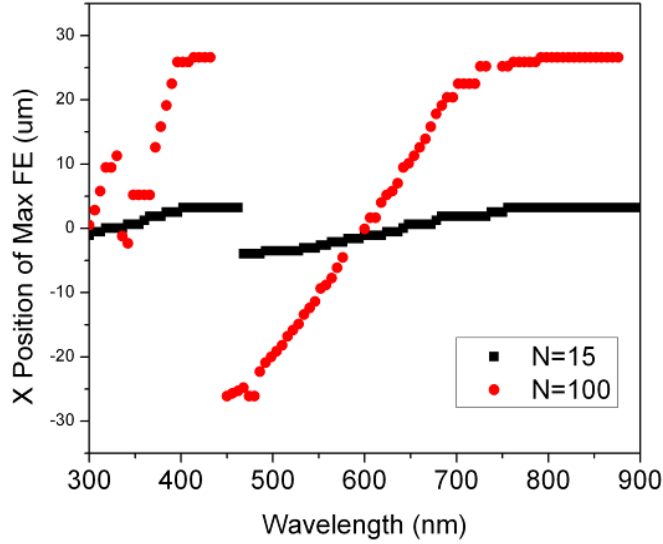


Fig 10. X position of the maximum field enhancement as a function of wavelength for both arrays, $N = 15$ and $N = 100$.

This work is currently being included in a paper to be submitted for publication.

2.5. Generalization of Photonic-Plasmonic Coupling

Using our CDA model, we have observed that we can design Wood's anomalies in which we couple long range photonic modes of periodic gratings to the enhanced localized surface plasmons (LSP) on quasi-statically coupled dimers. We have also observed that by chirping the lattice constant of the arrays we can create broadband coupling to these LSP. Additionally, further evidence of similar phenomenon has recently been published by this group [3]. In order to understand the relationship between the grating's spatial frequencies and the coupling to LSP in complex arrays we look as a first approximation at scalar Fourier optics. We start with the simple model which only allows propagating diffracted orders and look for the relationship between the wavelength and the characteristic length of the array to satisfy the Wood's anomaly condition for a normally incident scalar plane wave.

The general relation between the angles of the wavevector and spatial frequency of the wave is,

$$\begin{cases} \theta_x = \sin^{-1} \lambda \nu_x \\ \theta_y = \sin^{-1} \lambda \nu_y \end{cases} \quad (3)$$

When a plane wave is transmitted through a thin optical element with complex amplitude transmittance $f(x,y)$ which is a sum of many harmonic functions of different spatial frequencies, the transmitted optical wave is also the sum of an equal number of plane waves dispersed into different directions. Each spatial frequency is mapped into a corresponding direction in accordance with the spatial frequency condition (Equation 3). The amplitude of each wave is proportional to the amplitude of the corresponding harmonic components of $f(x,y)$ [4].

That is, for complex amplitude transmittance

$$f(x, y) = \iint F(v_x, v_y) \exp[-j2\pi(v_x x + v_y y)] dv_x dv_y \quad (4a)$$

the transmitted wave is,

$$U(x, y, z) = \iint F(v_x, v_y) \exp[-j2\pi(v_x x + v_y y)] \exp[-jk_z z] dv_x dv_y. \quad (4b)$$

Where the complex envelope $F(v_x, v_y)$ is the Fourier Transform of $f(x, y)$ and $k_z = (k^2 - k_x^2 - k_y^2)^{1/2} = 2\pi(\lambda^{-2} - v_x^2 - v_y^2)^{1/2}$ [4].

In metallic diffraction gratings, Wood's anomaly occurs at the point when the first diffraction order propagates exactly in the plane of the array. That is when $k_z \rightarrow 0$. Applying this condition we find that,

$$k_z = 2\pi\sqrt{\lambda^{-2} - v_x^2 - v_y^2} = 0 \quad (5a)$$

$$v_x^2 + v_y^2 = \left(\frac{1}{\lambda}\right)^2 \quad (5b)$$

Equation 3b is the equation of a circle with radius λ^{-1} which is plotted in Fig 11. We will use this equation to calculate the conditions for partial Wood's anomalies in our arrays.

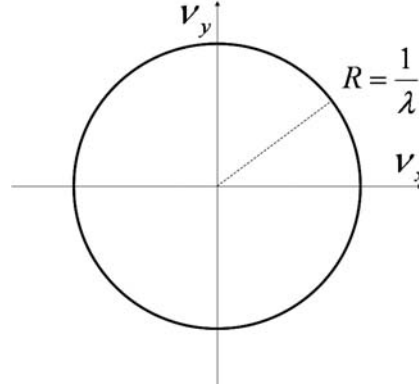


Fig 11. Condition for in-plane scattering

We now apply Equation 5b to our four standard arrays [3] to determine the efficiency of partial Wood's anomaly coupling. For a rough first order approximation we say that the complex amplitude transmittance $f(x, y)$ equals the array geometry so that $F(v_x, v_y)$ is the Fourier transform of the array. This is the case for a thin transparency but in reality is not the case for plasmonic metals because the field penetrates into the grating, altering the field distribution. Still it is a good first order approximation for engineering an array geometry, and conclusions drawn from it can be refined later. Fig 12 shows the Fourier transform of our four standard arrays: periodic, Fibonacci, Thue-Morse, and Rudin-Shapiro with the Wood's anomaly condition (Equation 5b) plotted for three wavelengths normalized to their characteristic length, a . In all four structures the characteristic length is the minimum center to center separation of the lattice which is the lattice constant of the periodic array.

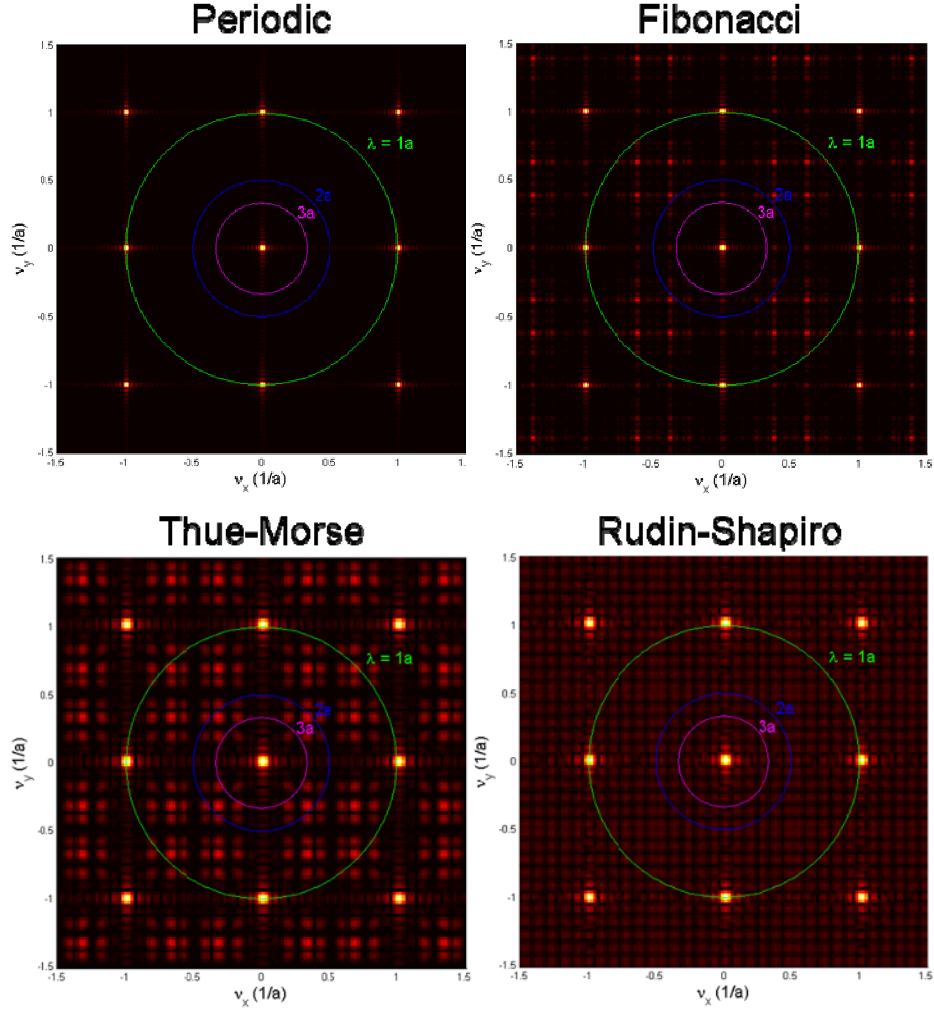


Fig 12. Wood's anomaly condition for (a) periodic, (b) Fibonacci, (c) Thue-Morse, (d) Rudin-Shapiro arrays at three different normalized wavelengths.

In Fig 12, the Wood's anomaly is clearly visible for the periodic array. For λ equal to the lattice constant the circle lies exactly on the first diffractive order and for λ greater than the lattice constant the only propagating order is the zero order. For the aperiodic arrays there are clearly a greater distribution of spatial frequencies and therefore the incident wave a partially couples into a Wood's anomaly like in-plane propagation at many frequencies to different extents.

In order to describe the efficiency of the grating to diffract a specific wavelength into in-plane propagating waves, we define a radial distribution function,

$$RD(R) = \frac{\int_{R-\frac{\Delta R}{2}}^{R+\frac{\Delta R}{2}} |F(R)| dR}{\int_0^R |F(R)| dR} \quad (6)$$

Which is depicted in Fig 13.

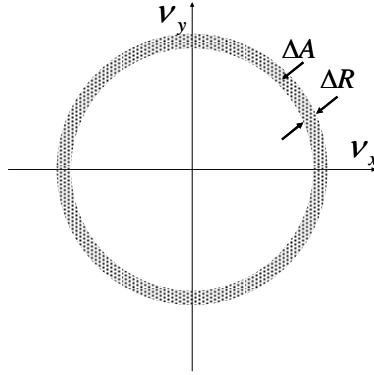


Fig 13. Graphical description of radial distribution function

The most important part of Equation 6 is the normalization. Since we are only considering the coupling of the wave to propagation orders only spatial frequencies inside the Wood's anomaly circle can be considered. This means as we change the wavelength we not only change the coupling to the in-plane propagating diffractive order but to all propagating orders because we change the number of orders which are allowed. The effect that this condition has on the distribution function can most clearly be seen if we look at the numerator and denominator separately for each of our four arrays. This is shown in Fig 14. The comparison of the distribution function for the four different arrays is shown in Fig 15.

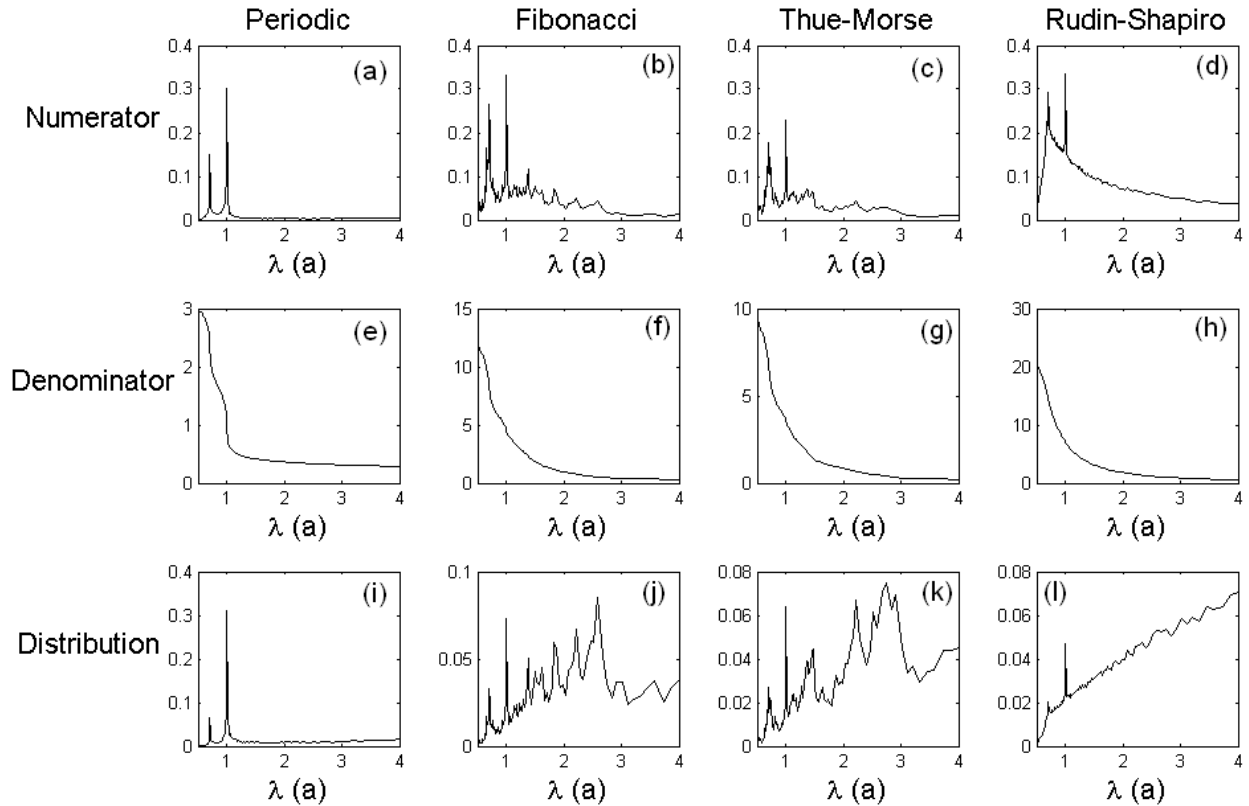


Fig 14. The components of the radial distribution function. (a-d) numerator, (e-h) denominator, (i-l) entire radial distribution function

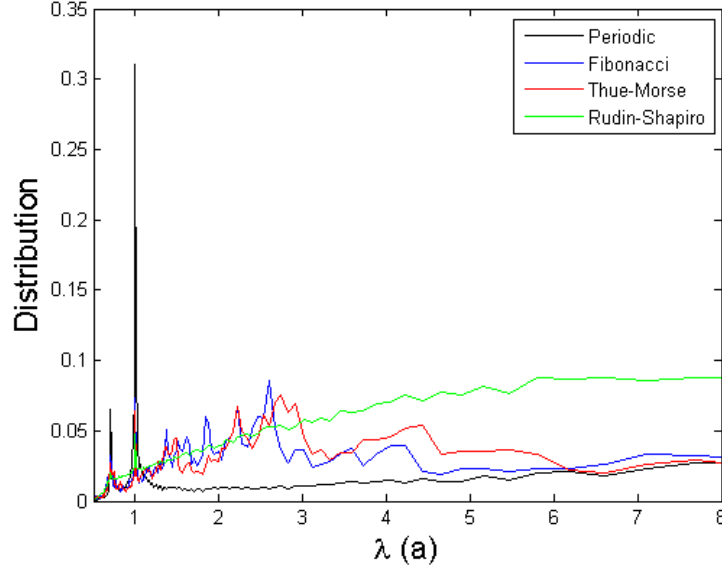


Fig 15. Radial distribution function of four arrays

Figs 14 and 15 show that for the periodic array there is a large amount of diffraction into the plane when $\lambda = a$, which corresponds to the first diffracted order and is the standard condition for the Wood's anomaly. There is an additional weaker peak at $\lambda = (2/3)a$ which corresponds to the second diffracted order. In the sub-wavelength region $\lambda > a$, there is no in-plane diffraction because only the zero order propagates. However, for the aperiodic arrays there are coupling pathways in the sub-wavelength region. These pathways appear to be dominated by the quasi-periodic arrays (Fibonacci and Thue-Morse) in the near sub-wavelength region ($1a < \lambda < 4a$) and the non-periodic array (Rudin-Shapiro) with a flat Fourier transform in the deep sub-wavelength region ($\lambda > 4a$). For a comparison in our experiments we typically use lattice constants around $a = 100$ nm to 300 nm for $\lambda = 532$ nm, $1.773a < \lambda < 5.32a$ and for $\lambda = 785$ nm, $2.617a < \lambda < 7.85a$.

Portions of this work will be included in future papers on aperiodic plasmonic arrays.

3. Experimental Activities

3.1. Depolarization Ellipsometry

We experimentally measure depolarization from periodic arrays of plasmonic dimers using spectroscopic ellipsometry. We show that at the Rayleigh cutoff, the depolarization has a sharp peak due to an increase in angularly dispersed scattering. We find that depolarization is maximized when the Rayleigh cutoff overlaps with the peak of the plasmon resonance of the isolated dimer. Results are confirmed with rigorous T-matrix simulations.

Fig16 shows the experimental geometry and results. (a) shows the experimental geometry. Dimers which are strongly coupled in the near field are arranged into a periodic lattice which provides diffractive coupling to the localized surface plasmon resonance. (b) shows the measured ellipsometry Ψ and Δ coefficients which agree with previously published data on these types of arrays [2]. (c) shows the depolarization spectra for an array of dimers and a comparable array of monomers. The dimers produce a dramatically larger depolarization than do the monomers. (d) shows that the strength of the depolarization varies with the minimum interparticle separation with more closely spaced dimers depolarizing the field more.

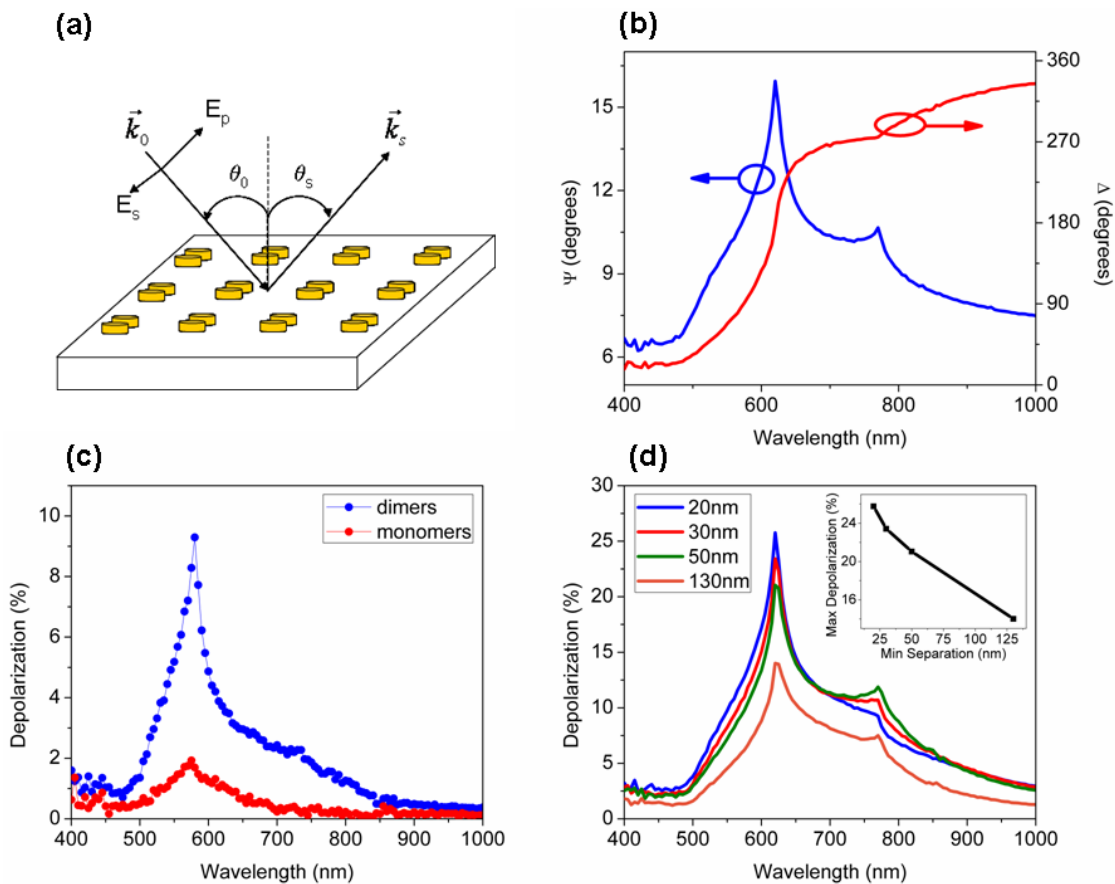


Fig 16: (a) Schematic of ellipsometry experiment. (b) Ellipsometric parameters Ψ and Δ for an array of gold dimers illuminated at 60° . (c) Depolarization of an array of dimers and monomers. (d) Depolarization of arrays of dimers with various minimum inter-particle separation indicated in the legend. Scaling of maximum depolarization with minimum separation (inset).

From a review of literature of ellipsometry of rough surfaces we determined the origin of the depolarization we measured was spatial as opposed to temporal [5]. We modelled this with the T-matrix method [1,6] by calculating a spatially averaged Stoke's vector over a solid angle Ω about the specular direction. The T-matrix method is used to calculate the Mueller matrix at N_Ω discrete angles over the Ω . The elements of the average Mueller matrix $\langle M \rangle_\Omega$ are $\langle m_{ij} \rangle_\Omega = \frac{1}{N_\Omega} \sum_{n=1}^{N_\Omega} m_{ij}^n$ and average Stoke's vector is found from this and the incident Stoke's vector $[I_0 \ Q_0 \ U_0 \ V_0]^T$ by,

$$\begin{bmatrix} \langle I \rangle_\Omega \\ \langle Q \rangle_\Omega \\ \langle U \rangle_\Omega \\ \langle V \rangle_\Omega \end{bmatrix} = \langle M \rangle_\Omega \begin{bmatrix} I_0 \\ Q_0 \\ U_0 \\ V_0 \end{bmatrix}. \quad (7)$$

The degree of polarization of the spatially averaged field is then,

$$P_\Omega = \sqrt{\frac{\langle Q \rangle_\Omega^2 + \langle U \rangle_\Omega^2 + \langle V \rangle_\Omega^2}{\langle I \rangle_\Omega^2}} \quad (8)$$

And the percentage of depolarization is $\Delta_{dp\Omega} = 100\%(1 - P_\Omega^2)$.

The results of simulations of chains of dimers with various minimum interparticle separation d_{\min} are shown in Fig. 17. (a) shows that the depolarization peaks when the grating mode overlaps with the localized surface plasmon resonance and that the amplitude varies with minimum particle separation. (b) shows the scaling of maximum depolarization with minimum separation. The data is fit by a logarithmic regression with $R^2 = 0.9965$.

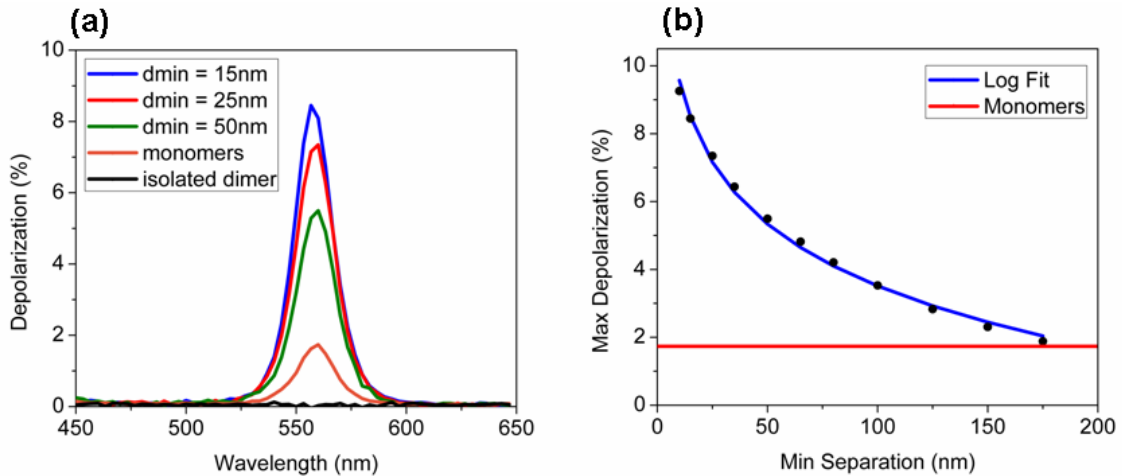


Fig 17. (a) Simulated depolarization for chains of dimers with various separation compared to that of monomers and an isolated dimer. (b) Scaling of the maximum depolarization with minimum separation.

This work is the subject of a paper which will be submitted to Nano Letters [publications 3]. This manuscript includes further details for an analysis of the effect of the angle of incidence.

3.2. Optical Limiting

We have started a set of optical limiting experiments at Natick to use designed planar plasmonic arrays to lower the input power and increase the switching rate of azobenzene doped liquid crystal cells similar to results previously reported by Osgood et. al. [7] for dispersed carbon nanotubes. We are using three array types representing three different classes of design strategies we have pursued. Examples of the electron beam fabricated arrays are shown in Fig 18.

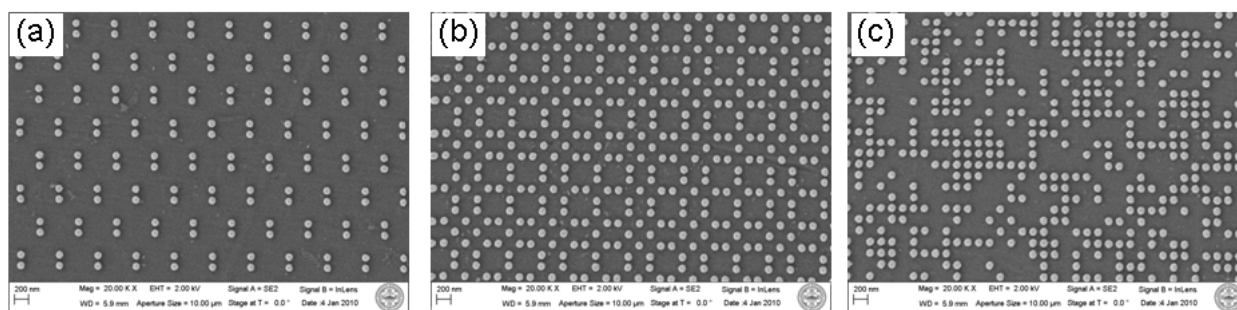


Fig 18. SEMs of 100 nm gold cylinder arrays of quartz. (a) triangular dimer with 530 nm lattice constant, (b) Fibonacci, (c) designed structure with particle swarm optimization.

We made three liquid crystal cells two of which had arrays of gold particles and one of silver. We attempted to perform two time resolved experiments. First a pulsed pump probe experiment in which the time dynamics of the polarization of a continuous wave (CW) 690 nm laser probe is measured as a 5 ns high fluence 532 nm Nd:YAG laser pump induces a switch in the liquid crystal from its nematic to isotropic state. A diagram of the experimental setup is shown in Fig 19 (a). Next the time dynamics of the limiting of a CW 530 nm laser were measured from the opening of a mechanical shutter until the liquid crystal (LC) had entirely switched phase. A schematic of this setup is shown in Fig 19 (b).

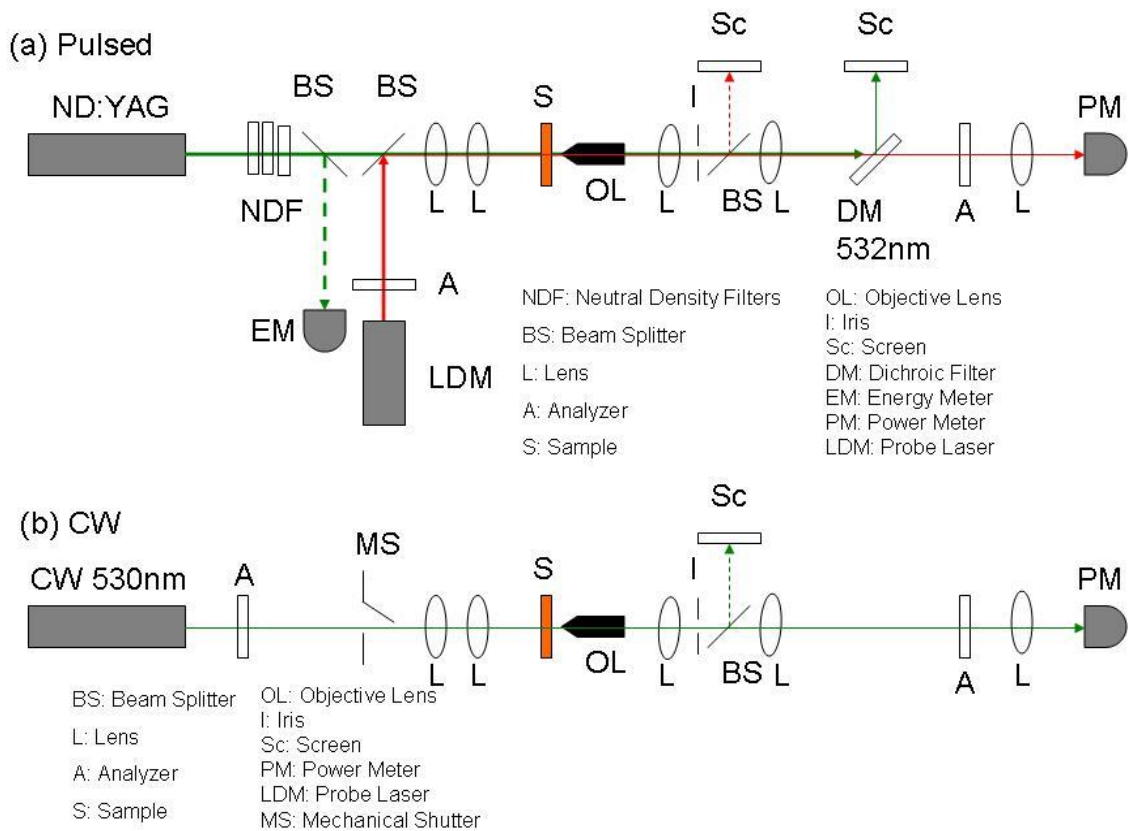


Fig 19. Schematics of limiting experiments. (a) Pulsed pump-probe: the two analyzers are crossed. The LC sample rotates the polarization when it is in the nematic phase. Time dynamics of the CW probe laser are measured on the power meter as a single pulse from the pump laser caused the LC to transition to the isotropic phase leading to zero transmission through the cross analyzers. (b) CW limiting setup: the two analyzers are crossed. A mechanical shutter opens and the time dynamics of the transmission of the CW 530 nm laser are measured on the power meter as the LC switches from its nematic to isotropic phase.

Although successful in measuring the time dynamics using the pump probe set up, we could not see a significant difference when the arrays were present. Fig 20 shows results for a switch with one particular pump energy (which was not directly measured but is identified by use of a 0.4 optical density (OD) neutral density filter) for (a) the Fibonacci array, (b) no array, and (c) a side by side comparison. The switching in these measurements goes from low to high. Although there appears to be an increase in the switching rate for the Fibonacci array it must be noted that the transmission starts at a higher value likely due to the depolarization effect from the highly scattering gold nano-particle array. An additional possible reason for this apparent effect is that the presence of the array could help the LC orient on the unrubbed surface. However the most important observation made about these samples, which influences the interpretation of the results, is that they are very non-uniform. This was determined by placing them between cross polarizers and illuminating from the back with unpolarized white light. As the sample is rotated with respect to the polarizers the transmission varies inconsistently throughout the sample. This will be further addressed in the section on our new experimental strategy.

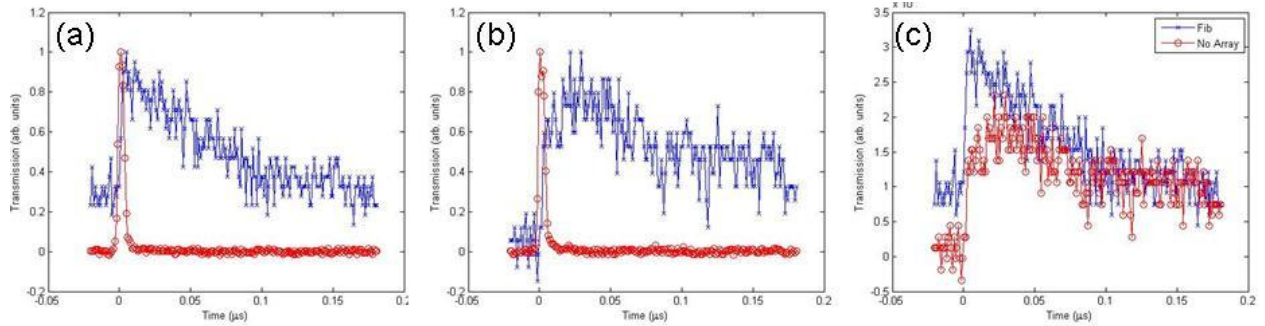


Fig 20. Pump-probe results. (a) Fibonacci array, (b) no array. Pump red, probe blue. Probe normalized to its maximum. (c) comparison on probe from (a) & (b) in unnormalized units.

No results for any of the three samples were attained for the CW experiment because the absorption of our samples was too high and no signal whatsoever could be measured. Fig 21 shows the OD of four samples as a function of wavelength. Samples 1 and 2 have gold arrays and were filled at Natick. Sample 3 has silver arrays and was filled by us. These are compared with an existing sample of identical specifications. The difference between our samples and this existing one is that for the existing sample the top and bottom substrates were pushed and rubbed together before sealing in order to remove excess dye which makes the cell thinner and lowers the absorption. This is not possible with our sample since rubbing them back and forth will destroy our arrays. If we can make cells with thicknesses at least as thin as this sample we will be able to perform CW experiments. Fig 22 shows the results of the CW limiting experiment for the existing sample in which the input power varied. It is clear that the switching rate increases for higher powers. This is consistent with the results in [7].

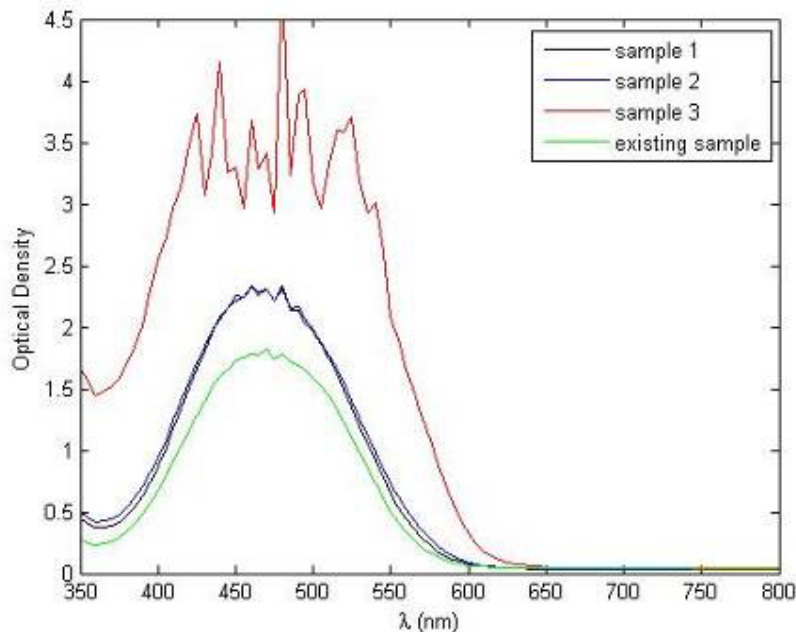


Fig 21. Optical density of four LC samples. Samples 1 and 2 have arrays and were made for us by Natick. Sample 3 has arrays that we made. The existing sample was made by Natick by rubbing back and forth to remove excess dye.

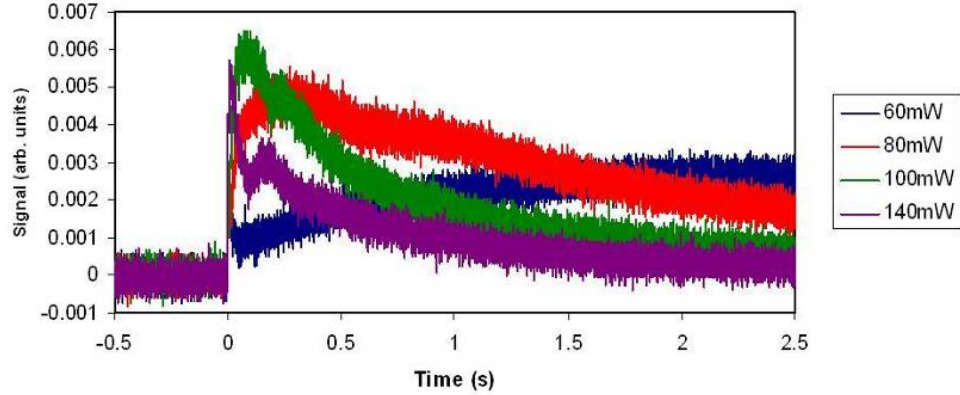


Fig 22. Time dynamics of CW limiting experiments from the existing sample. Input power is changed.

Our current inability to control the thickness and uniformity of the LC cells makes it impossible for us to perform the CW experiments and interpret the pulsed experiment. Further, it will not be possible measure any effect if the cells are too thick so that the amount of optically active material in the region of high field enhancement close to the array is a very small fraction of the entire LC volume. Our new strategy for these experiments will be to build a micro-fluidic channel around the arrays so as to better control the thickness and uniformity of the LC. The steps for fabricating the micro-fluidic channel are shown in Fig 23 and outlined below.

- (1) Define the area of the channel with photolithography on a silicon substrate, develop and pour PDMS (a hydrophilic polymer) over the area.
- (2) Peel off hardened PDMS.
- (3) Remove photoresist residue.
- (4) Nano-imprint a periodic grating into the channel for the LC to align with.
- (5) Place and clamp PDMS channel over plasmonic arrays and make pin holes for injection of LC.
- (6) Connect a syringe pump via tubing to the pinholes and fill the array with LC.

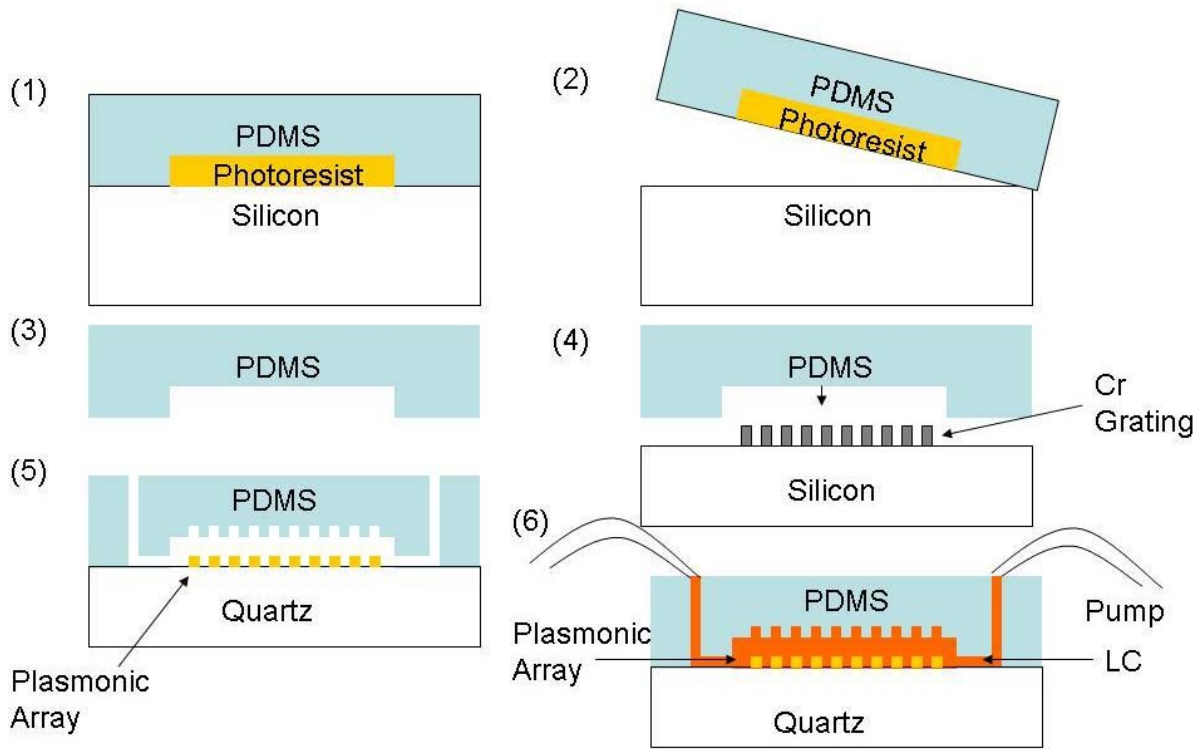


Fig 23. Steps for fabricating micro-fluidic channels around plasmonic arrays.

We have constructed several micro-fluidic channels using PDMS. Fig 24 shows (a) the photoresist mold to make the PDMS channel, (b) the PDMS channel on a quartz substrate and (c) arrays of Cr nanoparticles inside the PMDS channel. The channel is 18 μm tall as measured with a profilometer. We are planning to make thinner and more sturdy channels using diluted photoresist and spin on glass in place of PDMS.

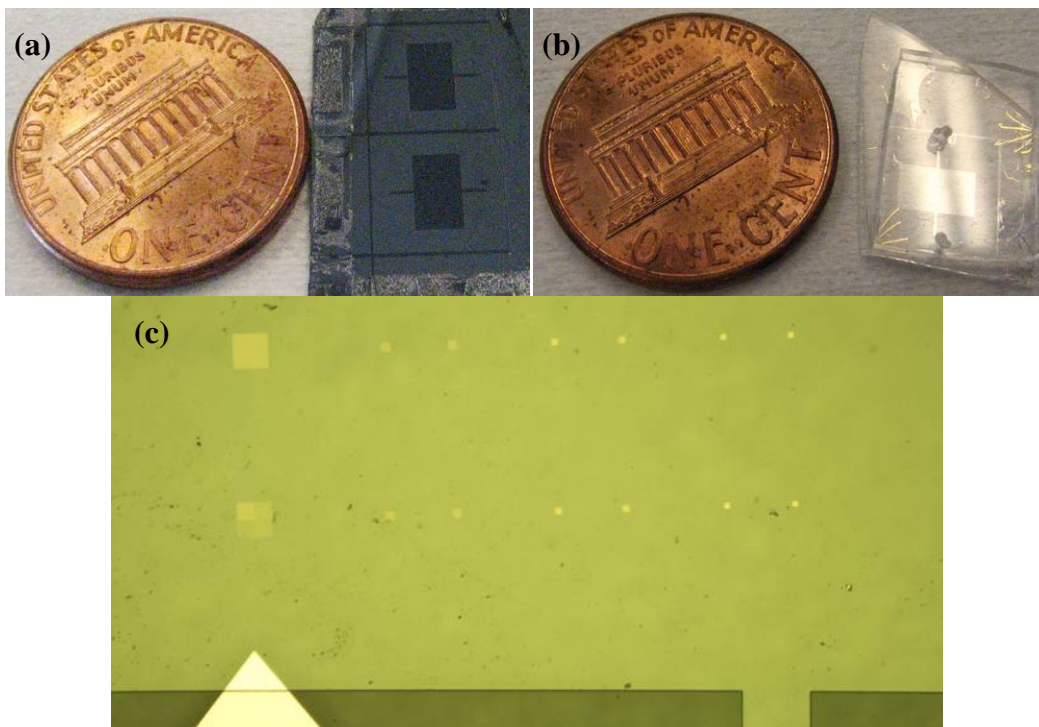


Fig 24. (a) Photoresist mold to make the PDMS channel. (b) PDMS channel on a quartz substrate. (c) Arrays of Cr nanoparticles inside the PMDS channel.

3.3. Enhancement of Kerr Nonlinearities in Azobenzene Doped Polymers

We have been working on producing uniform thin films of four third order-nonlinear Kerr effect dyes in a PMMA host. These include two azobenzene dyes, Disperse Red 1 (DR1) and Methyl Orange (MO), as well as two others Poly(1-vinylnaphthalene) molecular weight 30,000 (Poly-30k) and Poly(1-vinylnaphthalene) molecular weight 100,000 (Poly-100k). We abandoned the plan to dissolve the dyes and powder PMMA in chloroform because we were unable to obtain uniform films. Our new strategy involves dissolving the dyes in toluene and diluting Microchem PMMA 950 A5 electron beam lithography resist [1] with the toluene solution. We have had good success. Using a Woolman V-VASE ellipsometer we measured the thickness of the film made from a 1:1 mixture of PMMA (in anisole) to toluene spun at 2000 rpm for 45 s to be 214.765 ± 0.564 nm and 206.5 nm with a profilometer. We have made solutions of all four dyes which are 5% nonlinear dye by weight of solute (dye + PMMA) and 2.6% solute by volume in a 1:1 mixture of anisole to toluene. Fig. 25 shows the calibration curve for film thickness as a function of spin speed as measured with ellipsometry. As can be seen we have achieved films as thin as about 200 nm with this particular recipe. It should be noted that there are error bars on the plot but they are too small to be seen on this scale.

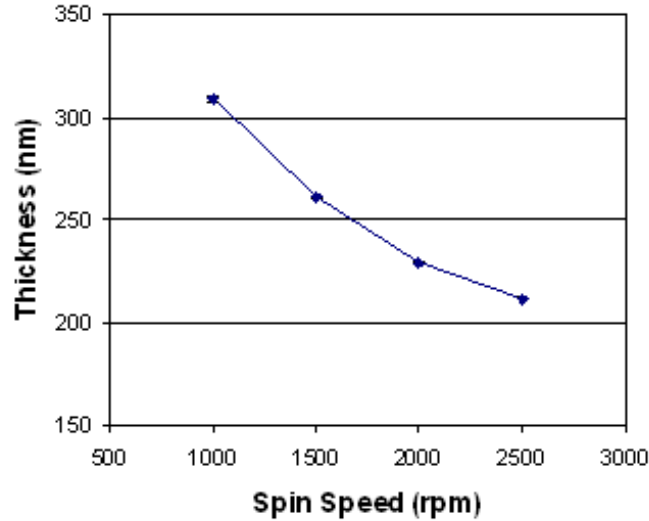


Fig 25. Spin speed calibration of 5% DR1, 95% PMMA by weight in a 2.6% solution of anisole:toluene 1:1

The principle method we are using to evaluate the nonlinearities of these films is zscan [8]. Zscan is a simple yet powerful technique for measuring the magnitude and sign of the nonlinear refractive index n_2 and the two-photon absorption coefficient β_2 . The basic setup we use is shown in Fig 26. A TEM₀₀ Gaussian laser beam is focused by a lens and a sample is moved by a motorized stage along the axis of the lens through the focus of the beam. This imparts on the beam a nonlinear phase shift which changes as a function of the sample's position z along the axis. The phase shift produces a known change in the far field pattern which can be sensed by placing an aperture on the axis of the beam before measuring its intensity with a power meter.

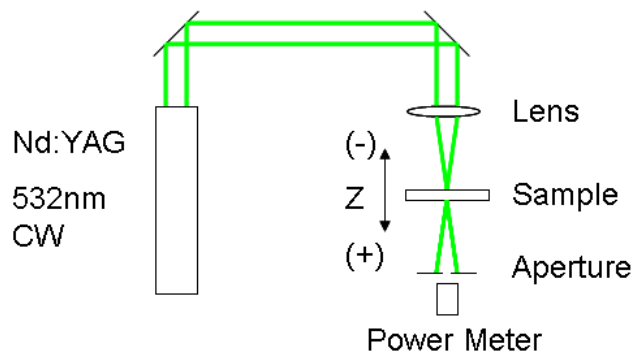


Fig 26. Zscan setup

For weak nonlinear phase shifts at the beam waist $\Delta\Phi_0$ the transmittance of the closed aperture experiment is known to fit the form [8],

$$T(z) = 1 + \frac{4\Delta\Phi_0 x}{(x^2 + 1)(x^2 + 9)} \quad (9)$$

where, $x = z/z_0$ and z_0 is the confocal parameter of a Gaussian beam. The approximate variation between the transmittance at the peak and valley is (ΔT_{pv}), and the distance between the peak and valley (Δz_{pv}) is [8],

$$\Delta T_{pv} = 0.406 |\Delta\Phi_0|, \quad (10a)$$

$$\Delta z_{pv} = 1.72 z_0. \quad (10b)$$

$\Delta\Phi_0$ is related to the nonlinear index as [8],

$$\Delta\Phi_0 = n_2 L_{eff} I_0 \quad (11)$$

where $L_{eff} = [1 - \exp(-\alpha L)]/\alpha$ is the sample's effective length and I_0 is the laser intensity at the beam waist. The nonlinear index can be either positive (n increases with increased intensity) or negative (n decreases with increased intensity). Fig 27 shows the theoretical closed aperture zscan transmittance (Equation 9) for both positive and negative values of n_2 .

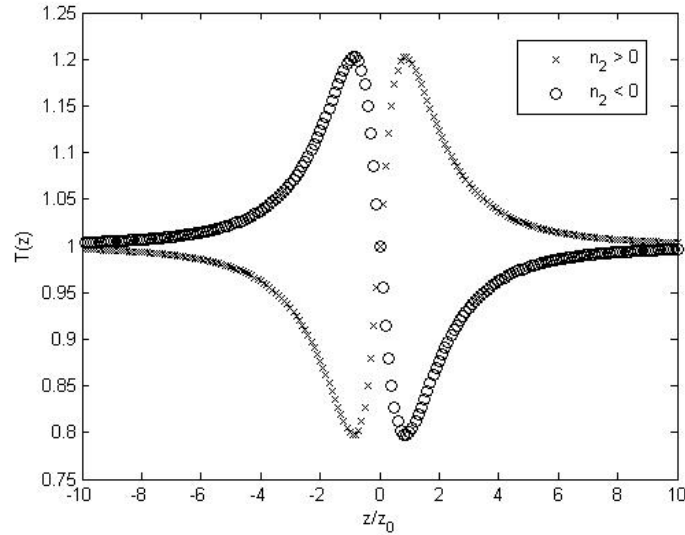


Fig 27. Theoretical closed aperture zscan data

We were unable to obtain zscan data from the azobenzene doped PMMA samples previously. We believe the films were too thin (200 nm) and the concentration of azobenzene was too low (5% by weight) to see an effect. We have made thicker samples with higher concentrations. The films are 5, 10, and 20% Disperse Red 1 (DR1) by weight. The DR1 was dissolved in Microchem PMMA 950 A5 electron beam lithography resist [9] without additional dilution. The solutions were spin coated at 1000, 2000, and 3000 rpm on quartz substrates and baked at 90° C for 15 min. The thickness of these films has not been measured, but based on measurements of the resist without DR1 it should be greater than 500 nm. We performed

spectrophotometry measurements of the linear absorption of these samples. Fig 28 shows the optical density of samples with different concentrations of DR1 spun at different speeds. It shows that there is a peak in the linear absorption at 490 nm. This resonance is where the trans-cis photoisomerization occurs which gives rise to the highest nonlinear change in the refractive index [10].

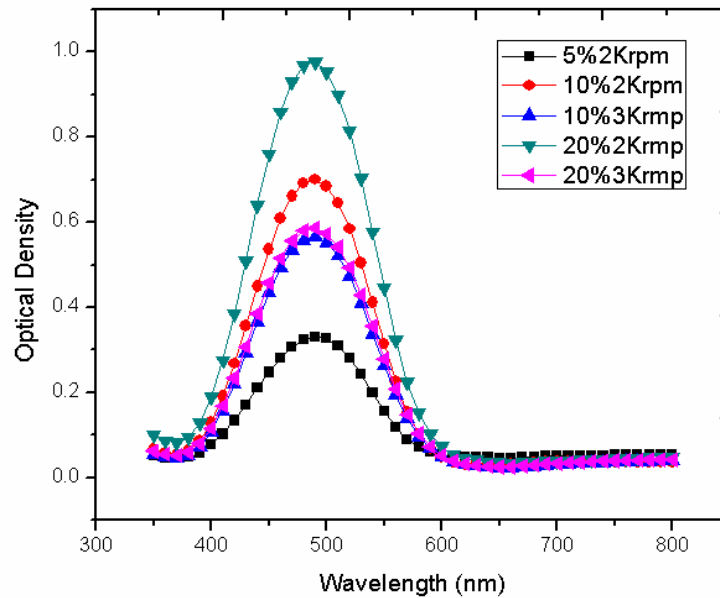


Fig 28. Optical density measurements of the DR1 doped PMMA films

We performed zscan measurements with our Ti-Sapphire laser at 800 nm with pulse widths of 200 fs. Un-normalized results are shown in Fig 29. This curve is characteristic of a negative n_2 as is expected from azobenzene [10].

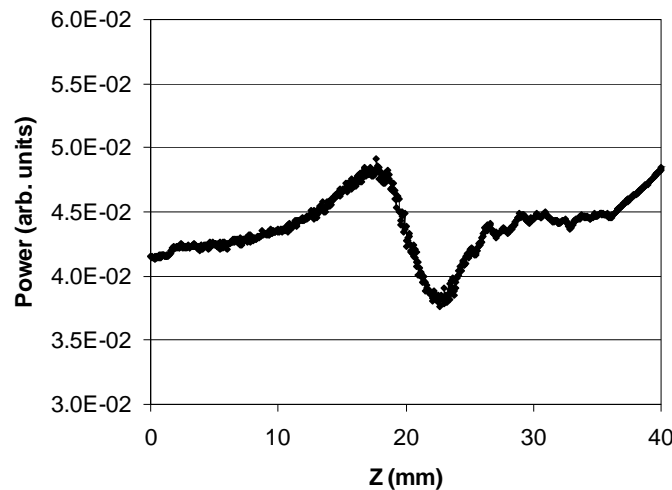


Fig 29. Un-normalized zscan data from DR1 doped PMMA film

4. Instruments

4.1. Scatterometer

We have built a scatterometer (also known as a polar nephelometer) for measuring angular scattering properties of lithographically defined microscopic arrays of nanoparticles. Instruments of this kind have been used for measurements on random ensembles and single particles. Collections of particles behave very differently than isolated ones; however, random orientation and position creates an averaging out of angular scattering properties. In our research we design particle arrays with complex ordering which gives rise to unique scattering properties. To the best of our knowledge this will be the first scatterometer capable of probing microscopic arrays of nanoparticles in well controlled positions. This will give us the capability to measure angular scattering intensity, polarization dependence on angular scattering, coherent back scattering, extinction, and bright and dark field images.

The instrument is shown schematically in Fig. 30 and pictures of various components are shown in Figs 31-34.

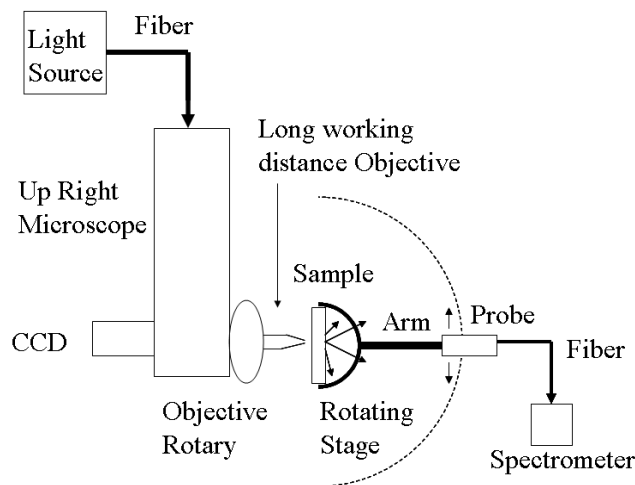


Fig 30. Schematic of scatterometer

The system consists of a side microscope which was custom-built for our laboratory which allows us to perform bright and dark field imaging with a calibrated true color CCD and spatially selective dark field spectroscopy with a monochromator and photon multiplying tube. The system was modified to add a fiber coupled probe on an automated rotating arm. The fiber couples the scattered light to a spectrometer. With this system we are able to measure the angular scattering spectrum of arrays of nanoparticles. An image of the system is shown in Fig 31.

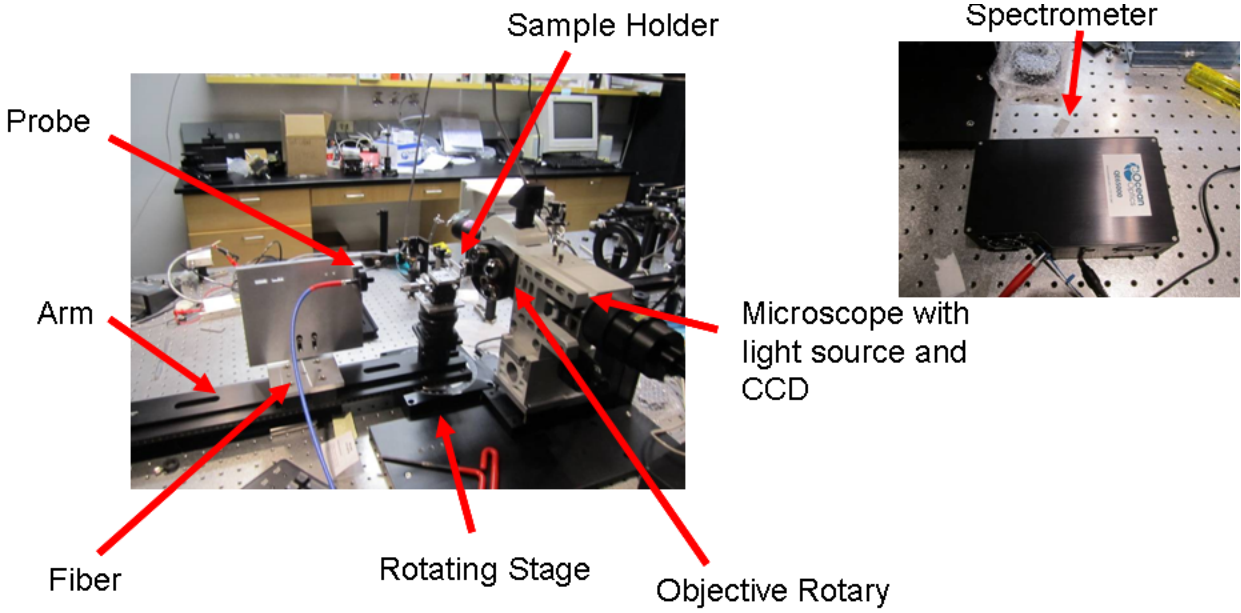


Fig 31. Scatterometer full system

The automated rotational stage moves the detection arm around the sample as is shown in Fig 32.

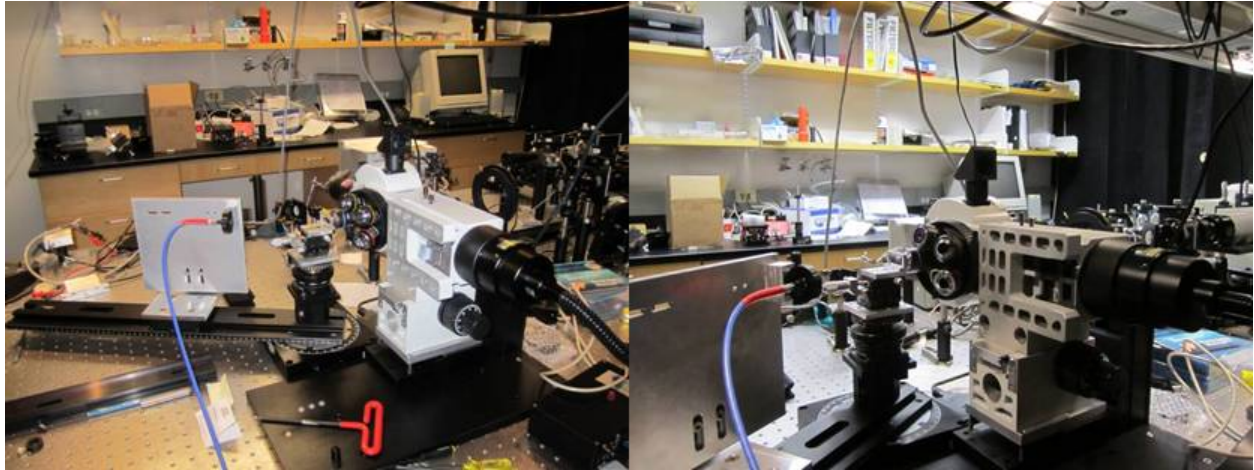


Fig 32. Automated variation of collection angle

The system may also be used with an automated rotating analyzer (a polarizer on the collection side). This can be used with a polarizer on the excitation side (inside microscope) to determine the change in the angle of polarization by the sample or without the polarizer to determine the bi-attenuation of the sample. The system with the rotating analyzer is shown in Fig. 33.

Automated Rotating Analyzer

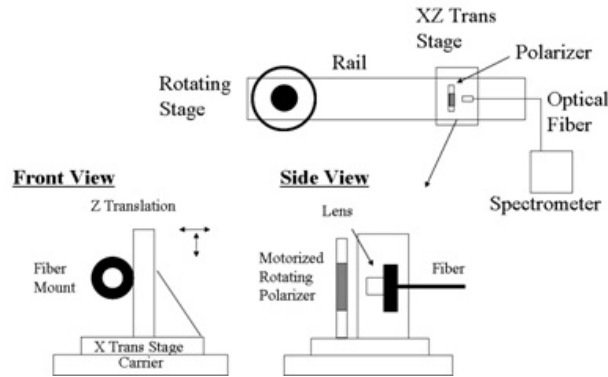
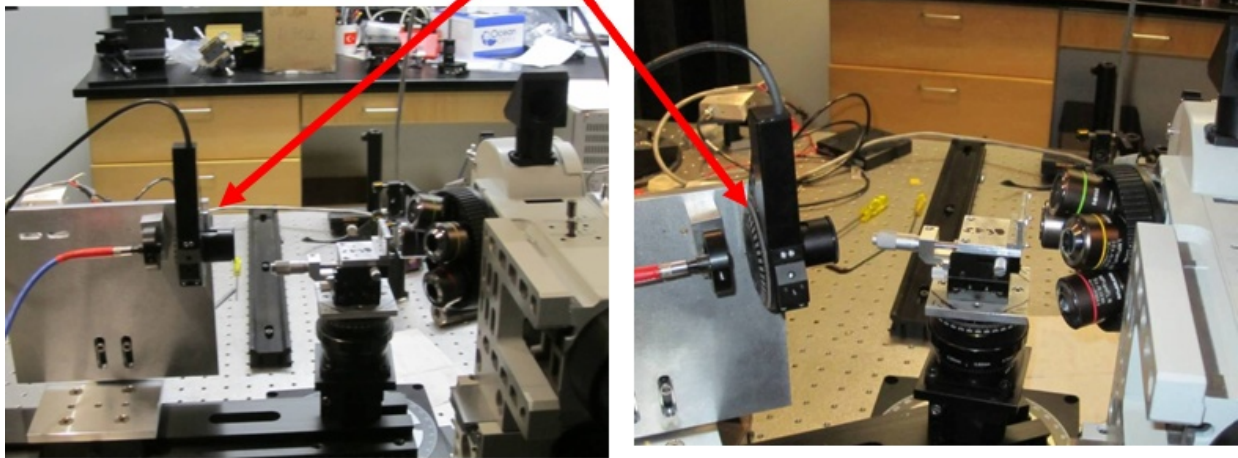


Fig 33. System with automated variable analyzer

Finally, the system can also be used with an automated liquid crystal variable phase retarder to dynamically change the state of polarization of the scattered light. This allows for the determination of the full elliptical state of polarization of the scattered light. The system with the variable phase retarder is shown in Fig 34.

Rotating Analyzer

Liquid Crystal Variable Phase Retarder

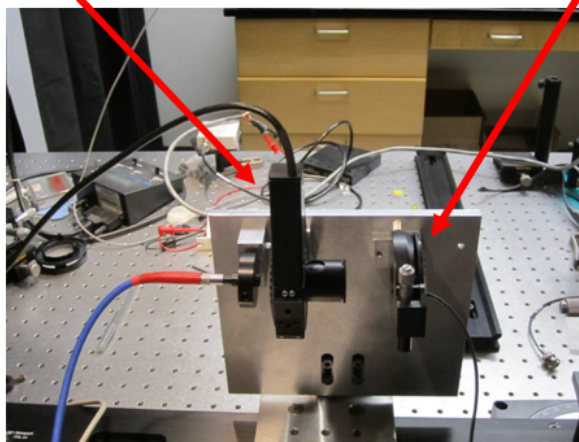


Fig 34. System with automated variable phase retarder

Publications

- [1] C. Forestiere, G. Walsh, G. Miano, L. Dal Negro, *Nanoplasmonics of prime number arrays*, Opt. Ex. Vol. 17, No. 26, pp. 24288-24303 (2009)
- [2] C. Forestiere, M. Donelli, G. Walsh, E. Zeni, G. Miano, L. Dal Negro, *Particle-swarm optimization of broadband nanoplasmonic arrays*, Opt. Lett., Vol. 35, Issue. 2. pp. 133-135 (2010)
- [3] G.F. Walsh, C. Forestiere, L. Dal Negro, "*Plasmon-enhanced depolarization of reflected light from arrays of nanoparticle dimers*", Optics Express, 19, 21, 21081 (2011)

References

- [1] C. Forestiere, G. Miano, S. Boriskina and L. Dal Negro, *The role of nanoparticle shapes and deterministic aperiodicity for the design of nanoplasmonic arrays*, Opt. Express 17, 9648-9661 (2009)
- [2] V.G Kravets, F. Schedin, A.N. Grigorenko, *Extremely Narrow Plasmon Resonances Based on Diffraction Coupling of Localized Plasmons in Arrays of Metallic Nanoparticles*, Phys. Rev. Let. 101, 087403 (2008)
- [3] L. Dal Negro, N.N. Feng, A. Gopinath, *Electromagnetic coupling and plasmon localization in deterministic aperiodic arrays*, J. Opt. A: Pure Appl. Opt. 10, 064013 (2008)
- [4] *Fundamentals of Photonics Second Edition* by B.E.A Saleh, M.C. Teich, Wiley, Chapter 4, (2007)
- [5] *Spectroscopic Ellipsometry* by H. Fujiwara, Wiley (2007)
- [6] *Light Scattering by Systems of Particles* by A. Doicu, T. Wriedt, Y.A. Eremin, Springer (2006)
- [7] R.Osgood III, D. M. Steeves, L. E. Belton, J. Welch, C. Quigley, R. Nagarajan, N. Tabiryan, S. Serak, G. Walsh, B. Kimball, *Optical Properties of Nanoparticle-doped Azobenzene Liquid Crystals*, MRS Proceedings 1142-JJ10-05 (2008)
- [8] M. Sheik-Bahae, A.A. Said, T.H. Wei, D.J. Hagan, E.W. Van Stryland, *Sensitive Measurement of Optical Nonlinearities Using a Single Beam*, IEEE J. Quant. Elect., vol. 26, no. 4, (1990)
- [9] "NANO™PMMA and Copolymer" Data Sheet, MicroChem Corp. (2001)

[10] L. Brzozowski, E.H. Sargent, "Azobenzenes for photonic network applications: Third-order nonlinear optical properties", *J. Mat. Sci: Mat. Elect.*, 12 (2001) 483-489